Journal of Applied Electrochemistry (2025) 55:603–617
https://doi.org/10.1007/s10800-024-02199-5

RESEARCH ARTICLE

Synthesis of green anode material for lithium-ion battery from orthodontic waste by fuzzy logic

Humza Ashraf[1] · B. Deniz Karahan[1,2] · Zekai Şen[3,4]

Received: 13 April 2024 / Accepted: 4 September 2024 / Published online: 18 September 2024

Abstract

For the fabrication of green batteries, instead of synthesizing the electrode materials from high-purity metal powders via primary production methods, it is of great importance to design and produce an electrode material by recovering valuable elements from existing wastes. In this article, for the first time in open literature, an electrode active material was fabricated from biomedical waste by using a combination of leaching and hydrothermal methods. Once 100% leaching efficiency was achieved, an optimization was realized in the hydrothermal parameters (filling ratios, time, and temperatures) to fabricate spherically shaped metal oxide powders with 150 nm particle size. Innovatively, fuzzy logic modeling was used for refinement of parameters. Subsequently, three verification experiments were realized at optimum conditions, defined by fuzzy logic. The repeatability as well as the accuracy of the model was confirmed. In the meantime, analysis of variance (ANOVA) technique was applied for identification of the most effective parameter for the fabrication of powders in hydrothermal conditions. A detailed mechanistic analysis about the formation of particles was also realized. Finally, the possible use of this metal oxide powder as an anode material was evaluated galvanostatically and potentiostatically. The electrode delivered a higher capacity than graphite and achieved 100-cycle tests with success. The presented approach was anticipated to constitute an example for the future, as it brought an effective perspective to material scientists about the valorization of biomedical waste in high value-added applications such as energy storage devices.

✉ B. Deniz Karahan
bdkarahan@itu.edu.tr

[1] Research Institute for Health Sciences and Technologies (SABITA), Istanbul Medipol University, Beykoz, 34810 Istanbul, Turkey

[2] Department of Metallurgical and Materials Engineering, Istanbul Technical University, Maslak, 34469 Istanbul, Turkey

[3] Department of Civil Engineering, Istanbul Medipol University, Beykoz, 34810 Istanbul, Turkey

[4] Department of Climate Change, Energy and Health, Istanbul Medipol University, Beykoz, 34810 Istanbul, Turkey

Graphical abstract

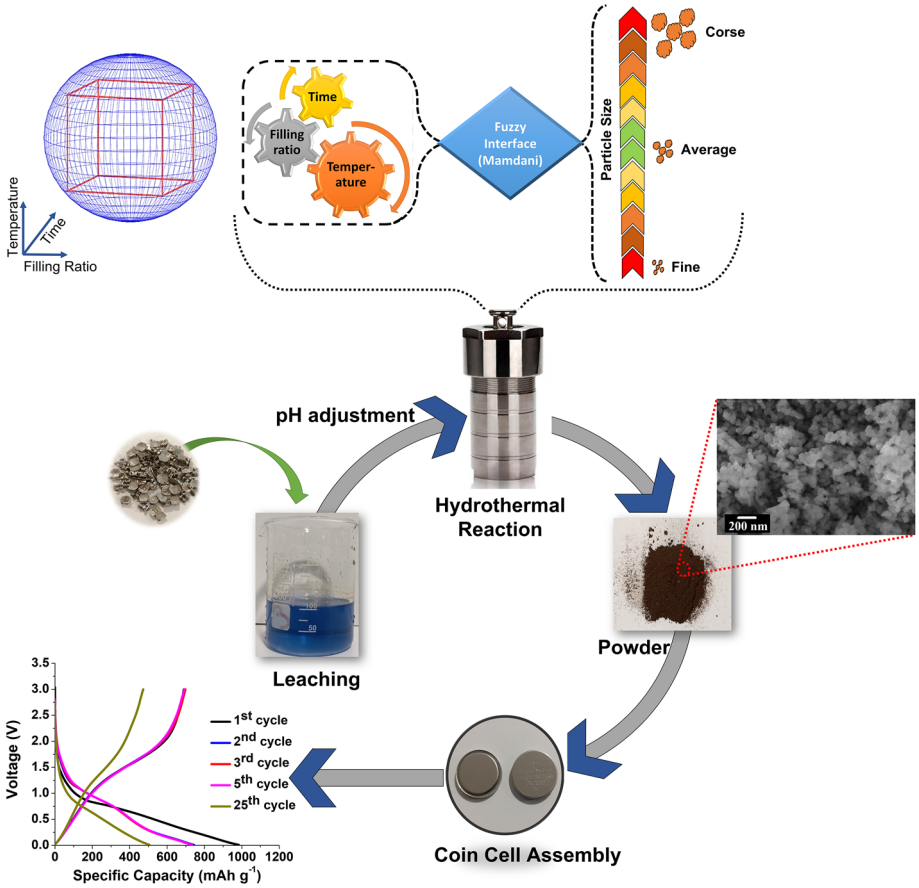

Keywords Orthodontic waste valorization · Waste to source · Fuzzy logic · Nanocomposite · Transition metal oxide anode

1 Introduction

In the twentieth century, the fast-growing population and economies need huge amounts of resources to fulfill the needs of consumers. With the current population growth rate, it is expected that by 2040, many of the natural resources are going to be consumed completely [1]. The continuous decrease in primary energy sources (i.e., fossil fuel) and fast-growing pollution necessitate the use of renewable energy along with energy storage facilities. Among alternatives, lithium-ion batteries (LIBs) are the most renowned ones, due to their lightweight, excellent energy density (> 150Wh kg^{-1}), lack of memory effect, low self-discharge rate, and long cycle life [2, 3].

LIBs are used in different sectors such as in the transportation (autocycle cycles, cars, busses, forklifts, etc.), electronic goods (laptops, personal care devices, phones, etc.), and stationary grid applications [2]. A report issued in 2020 states that by 2030 the energy stored in LIBs will surpass 2 TWh collectively [4]. In another report, it is estimated that the growing market of LIB is going to expand up to 300 billion US dollars by 2050, and per year power storage production requirement will be 4–12 TWh [5]. This makes it obvious that with the developing market, a higher amount of electrode material is needed for the fabrication of LIBs.

LIB consists of four basic components: electrolyte, separator, cathode, and anode [6, 7]. When the energy consumption of the LIB manufacturing process is considered, 163 kWh of energy is found to be utilized for the fabrication of LIB that stores 1kWh of energy [8, 9]. Detailed analysis reveals that 70–80% of that energy is used mainly for the electrode active material fabrication [10], which results in approximately 150 kg CO_2 emission (to store 1kWh of energy in LIB) [11, 12]. Moreover, the cost of active material covers 65% of the total production cost of the LIB [13]. Here, keeping in mind the market forecast of LIB with the purpose of revenue generation, the motivation is to reduce the production cost of active

material without compromising environmental safety. As a solution, some scientists have studied the recovery of metals from spent LIBs by pyro and hydrometallurgical processes [14]. Alternatively, mill scale [15], spent pickled acid [16], flue dust [17], and ash [18] from different furnaces are also utilized as the starting material, and valuable metals are recovered from them to be used in the fabrication of the electrode active material. In these studies, industrial waste usage in the synthesis of electrode active materials is not proposed only to offer solutions for the problems experienced during the disposal of the existing waste but also to reduce the environmental damage resulted from the synthesis of the electrode active material with the primary methods [19–21]. In 2019, Liu et al. [19] and Luo et al. [20] have fabricated hematite/C based hollow spindles and hematite/C based composites from acid pickle iron oxide, respectively. On the other hand, in 2018, Li et al. [21] have fabricated 200 nm sized carbon coated ferric oxide composites from waste toner. In all these studies, scientists prefer to synthesize submicron sized metal oxide/C composite since Wang et al. [22] reported that pure metal oxide anodes fail in early stage of galvanostatic test, because of their low electronic and ionic conductivities. Another challenge, faced by transition metal oxide, is the huge volume expansion occurrence in the anode active material in discharging [23]. This significant change in the volume of the anode active material during cycling causes electrode pulverization and rapid capacity decay, impeding their practical applications [24, 25]. To overcome this main demerit of volumetric expansion and to enhance structural stability of anode material, its particle size optimization is greatly emphasized by researchers. Many research efforts conclude that reducing the particle size (of anode material) to 150 nm or below provides a balance between stress accommodation ability as well as high surface area for better lithiation kinetics and eventually high capacity [26–29]. Likewise, Courtel et al. [25] have also shown in their study that for mixed transition metal oxide, as anode active material in LIBs, ~ 150 nm particle size is critical to counter stress during volume expansion and maintaining electrochemical performance. Furthermore, when nano-sized anode active material (< 100 nm) is utilized, the performance decreases over time during cycling due to the formation of "electrochemical induced agglomeration" which is urged by the high surface energy of nano particles [30–32]. Additionally, the production of a thicker SEI on the nano-sized anode active material results in higher resistance at the electrode/electrolyte interface, which lowers the anode's performance at high current loads [33, 34]. Therefore, optimization in the particle size is highly required since neither too low nor too big particle size of metal oxide leads to good cycle performance in the galvanostatic tests.

Up to now, mostly, researchers have optimized the electrode active material's properties by studying the effect of one parameter at a time. For example, Zhao et al. [35] used a full factorial design to optimize four factors with 2 levels to achieve a minimum particle size. Rangappa and co-worker [36] utilized full factorial design for optimizing the cooling system of the LIB considering 3 factors with 3 levels.

The orthogonal experimental design supports a hypothesis with a definitive answer (YES/NO or TRUE/FALSE) but disregards the 'possibilities' between these two distinct alternatives. In order to collect more data, it is possible to increase the number of trials in a crisp (two-value) logic system (by increasing the number of factors and their levels), which leads to an increase in the number of experiments runs for a finer orthogonal system. Therefore, such an approach might not be practically possible, especially when time, cost, or resource constraints are considered.

On the other hand, the use of fuzzy logic (FL) system inference-based modeling maximizes the fabrication efficiency of the particles at the desired properties with a smaller number of experiments because this alternative logic suggests an unorthodox approach which does not require many experiments and it allows for the analysis of complex systems' control, under the effect of independent parameter interactions [37–39]. Moreover, this flexibility makes FL modeling particularly suitable for problems where the relationships between variables are not precisely (crisply) pre-defined. There are two popular types of fuzzy inference systems as Mamdani [40] and Takagi-Sugeno [41] models. The qualitative form of data can be well modeled by Mamdani FL model, where inputs and outputs are related through fuzzy set inclusive rule bases. The superiority of FL modeling can be observed in cases where the design space is complex, and the interactions between variables are nonlinear or difficult to define precisely. FL modeling allows the incorporation of expert knowledge, linguistic variables, and logical rules, to enable a more intuitive and qualitative representation of the problem mechanism. Furthermore, FL modeling is capable of handling uncertainties inherent in real-world systems, providing robustness in decision-making and finding the optimum solution [42]. For example, Majmudar et al. [43] used FL to measure and study the size and shape of the fabricated gold particle by c-mean clustering approach on Transmission Electron Microscopy (TEM) images. Shetty et al. [44] practiced the Taguchi method with FL modeling to optimize and predict surface roughness of composite. Hosseini et al. [45] also applied FL model in their study, this artificial intelligence (AI) based approach enabled them to develop a relation between Cr (VI) removal efficiency (as output) and pH, contact time, initial Cr (VI) concentration, and absorbent dose as input variables by applying Mamdani interface system.

In this study, in order to exemplify the use of FL principles in the fabrication of green electrode material, innovatively, orthodontic waste (stainless steel braces) has been chosen as starting material. Biomedical sector as a growing market attracts attention as their waste contains 57%, 21%, and 6% amounts of Fe, Ti, and Ni, respectively. In 2020, the World Health Organization (WHO) [46] reported that 144,000 tons of biomedical waste were mostly discarded. So far, a couple of research groups have tried to recover metals from biomedical waste, but none of them have designed a procedure to manufacture LIB electrode materials out of it. Thus, in this study, firstly the leaching efficiency of stainless steel (SS) braces is maximized (not given here), then the hydrothermal reaction parameters (temperature, time, filling ratio) are heightened by FL modeling to achieve ~150 nm as the critical particle size for electrode material [29]. The fabricated powder is utilized as an anode material in lithium-ion batteries leading to promising results.

2 Experimental

2.1 Powder synthesis

Stainless steel braces were collected from local dentists near Istanbul, and they are washed at 60 °C for 2 h, and then leached by sulfuric acid. Here, leaching at 90 °C with 4 M H_2SO_4 for 4 h while maintaining a solid-to-liquid ratio of 1/50 in the reflux system results in 100% leaching efficiency. After applying 14 M NaOH to bring the leachate's pH to 10, the solution is transported to the hydrothermal reactor. The reaction is carried out at various filling ratios, time, and temperatures determined using FL modeling at this step. The precipitates are then separated and thoroughly cleaned by centrifuging it for 30 min at 4500 rpm. Precipitates are heated at 730 °C for 5 h in an air environment after drying at 100 °C for 12 h.

2.2 Fuzzy logic modeling

In this study, the refinement in particle size is realized by using FL principles by using a toolbox of MATLAB for further optimization and verification of the hydrothermal reaction parameters. In this regard, the three input variables, namely, time, temperature, and filling ratio are connected to one output (particle size), with Mamdani FL inference system model (see Table 1 and Fig. 1). The three inputs and output are fuzzified into three fuzzy sets linguistically as Gaussian function. Equation 1 represents the formula for fuzzifying the experimental numbers into Gaussian function [47], where σ is a standard deviation and c is the mean of the function. These three inputs with three fuzzy sets generate 27 fuzzy rules. These rules are then triggered according to fuzzy inference system (FIS) principles to obtain the output fuzzy set. The final numerical value was obtained after the defuzzification of this set according to centroid defuzzification approach [39]. Moreover, MINITAB software version 20 is used to analyze the experimental data and perform ANOVA analysis.

Table 1 Linguistic levels of Input and output of fuzzy logic model

Variable	Linguistic levels	Values
Temperature (°C)	Low	156
	Middle	181
	High	204
Time (h)	Less	13
	Intermediate	20
	More	25.7
Filling ratio	Small	0.3237
	Moderate	0.556
	Big	0.849
Particle size (nm)	Fine	155.7
	Average	258.1
	Coarse	410

$$f(x;\sigma;c) = e^{-\frac{(x-c)^2}{2\sigma^2}} \quad (1)$$

2.3 Materials characterization

2.3.1 Structural, morphological, compositional analyses

The chemical composition of the fabricated powder is examined by applying X-ray fluorescence (XRF, Rigaku—ZSX Primus II). To analyze the structural phases of the fabricated powder, an X-ray diffractometer (XRD, Brucker AXS/Discovery D2 phaser) is utilized between 10° and 90° by Cu Kα with 0.02° sec^{-1} scanning rate. The particle size is determined by Malvern Panalytical ZETASIZER ULTRA.

2.3.2 Cell fabrication and electrochemical characterization

For electrochemical evaluation of synthesized material in lithium-ion batteries, anodes are fabricated by mixing the electrode active material, conductive additive (TIMCAL C-64), and binder (PVDF; polyvinylidene difluoride) in an organic solvent (NMP: N-methyl pyrrolidone) with 60: 25: 15 ratios in Thinky ARE-250. The lamination is realized by coating the slurry on copper foil with the Dr. Blade technique [48]. Then, the coated foil (lamination) is dried (at 70 °C for 12 h and at 120 °C for 12 h), rolled, and punched.

Then, CR2032 standard coin cells are assembled in argon-filled glovebox MBRAUN, LabMaster (< 0.1 ppm O_2, < 0.1

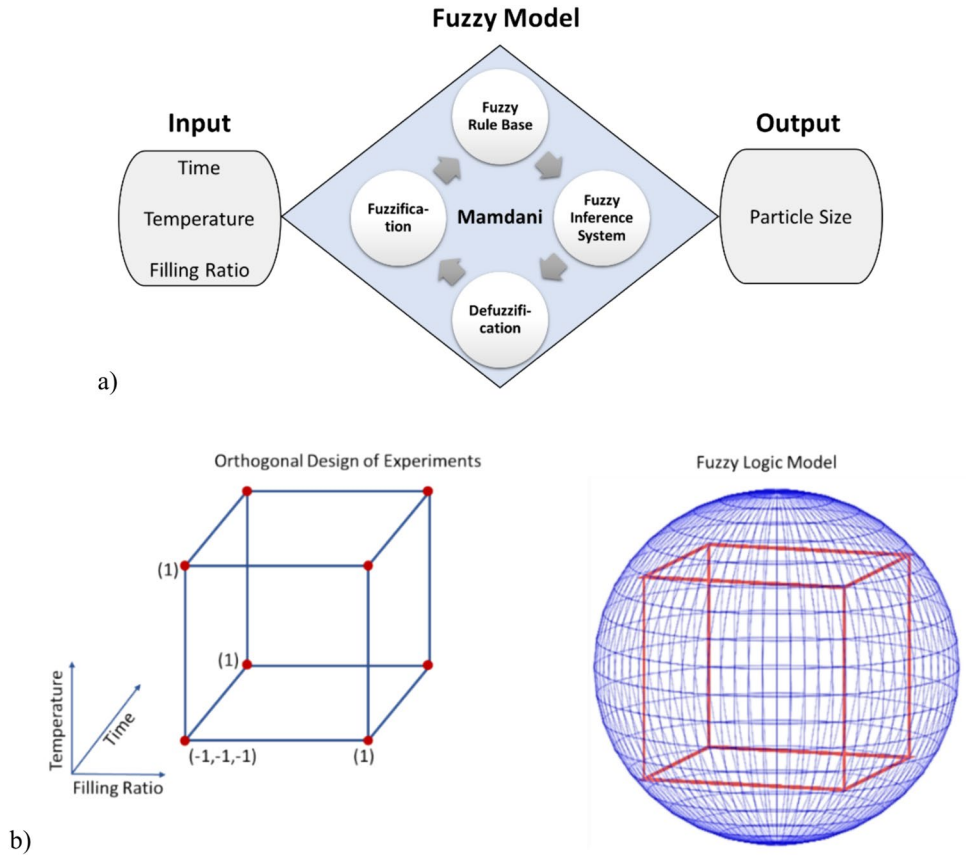

Fig. 1 **a** Structure of FL model with three inputs and one output, **b** Schematic demonstration about the difference of orthogonal design to FL model

ppm H_2O). The electrolyte contains 1M $LiPF_6$ in EC: DMC (1:1) solution. The separator is Celgard 2400. Galvanostatic performances' assessments are made at a current load of 50 mA g^{-1} between a voltage range of 1 mV–3 V (vs Li/Li^+) using the Neware Battery Analyzer System. The lithiation mechanism has been examined by performing cycling voltammetry using Gamry Interface1000E. The first 4 cycles of CV curvatures of each electrode are retrieved by cycling the electrodes between said voltages with a scan rate of 0.2 mV sec^{-1}. The electrochemical impedance spectroscopy (EIS) has been executed at 1 mV, from 0.01 Hz to 100 kHz in symmetrical cells using Gamry Interface1000E. The symmetric cell has been assembled following the procedure explained adopted by Burns et al. [49], typical cell contains an anode cycled to specific cycle and then discharged to 1mV vs the same but fresh electrode.

3 Results & discussion

3.1 Fuzzy logic (FL) modeling

This modeling deals not only with every parameter's effect but also with the interaction of parameters. It involves the subdivision of important factors affecting the input process and possible outcome (output), into linguistic fuzzy sets (Table 1). The linguistic fuzzy sets are the subsets of both input and output as "small", "intermediate", "less", "more", and "most," which are linguistic fuzzy words. The logical set of fuzzy rules-based relations is developed for each input variable simultaneously with fuzzy sets of the output variable. Each of the inputs and the output is fuzzified into 3 fuzzy subsets. Figure 2 shows the fuzzy subsets of both input and output. Table 1 indicates the central values of each Gaussian fuzzy function (see Fig. 1b). As

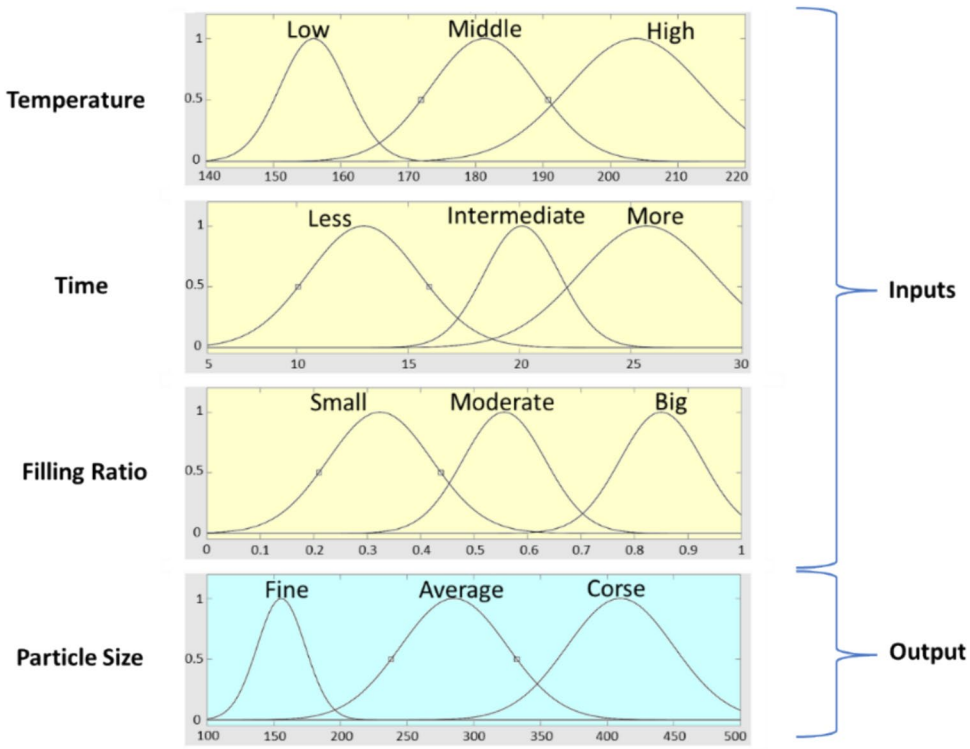

Fig. 2 Fuzzified inputs (Temperature, Time and Filling Ratio) and output (Particle Size) with their fuzzy subsets

Mamdani FIS is more appropriate to apply on practical experimental works, hydrothermal parameters to fabricate particle size around 150 nm are adjusted accordingly.

Validation of fuzzy model

Many studies have been reported to optimize the particle size of metal oxide material in hydrothermal reactions [50–53]. In this study, time, reaction temperature, and filling ratio of the reactor have been chosen as parameters to control the morphology and the size of forming powder with 3 levels for each of them. As a result, 27 possible combinations are proposed as fuzzy rule base (see Table 2), but not all the experiments need to be performed, unlike the orthogonal design of experiments (Figs. 1b and 3a). Therefore, by taking most logic experiments and their results, FL model enables to develop a strong relation between the inputs and the output. This attribute gives superiority to FL modeling over conventional orthogonal experimental designs.

The output obtained in Mamdani type FIS is in the form of fuzzy set, which needs to be de-fuzzified into one crisp numerical value. In this study, the fuzzy set is de-fuzzified by centroid method by taking the centered value of the fuzzy output set (Fig. 3a). The FL model is validated by calculating the percentage relative error (PRE) and sum of square error (SSE) between the model prediction and the experimental values using the following Eqs. 2 and 3 [54].

$$\text{Percentage Relative Error (PRE)} = \frac{(V_{i,E} - V_{i,C})}{\max(V_{i,E}, V_{i,C})} \times 100 \tag{2}$$

$$\text{Sum of Squared Errors (SSE)} = \sum_{i=1}^{n} \left(\frac{(V_{i,E} - V_{i,C})}{\max(V_{i,E}, V_{i,C})} \right)^2 \tag{3}$$

$$\text{Root Mean Squared Errors (RMSE)} = \sqrt{\left(\frac{\sum_{i=1}^{n} (V_{i,E} - V_{i,C})^2}{n} \right)} \tag{4}$$

Here, V_E is the experimental particle size value and V_C is the calculated particle size value through the FIS model. Approximately, the error percentage is found as ~ 2% and this is within the practically acceptable engineering error limits of ± 5%. By using Eq. 4 [54], the calculated root mean squared error (RMSE) is found to be 0.144. As the RMSE value is very close to 0, it indicates the goodness of the model.

Moreover, Fig. 3b displays the experimental and the model prediction values of particle size. For 150 nm particles, the refined parameters of the FL model are 150°C temperature, 12 h, and 100% filling ratio. Three experiments are carried out under these circumstances, and the particle sizes of these trials are measured for the confirmation and the validation of the parameters adjustment. The

Table 2 Linguistic relation between levels of input and output

	Time	Temperature	Filling ratio	Particle size
Rule 1	Less	Low	Small	Average
Rule 2	Intermediate	Low	Small	Average
Rule 3	More	Low	Small	Average
Rule 4	Less	Middle	Small	Corse
Rule 5	Intermediate	Middle	Small	Corse
Rule 6	More	Middle	Small	Corse
Rule 7	Less	High	Small	Corse
Rule 8	Intermediate	High	Small	Corse
Rule 9	More	High	Small	Corse
Rule 10	Less	Low	Moderate	Average
Rule 11	Intermediate	Low	Moderate	Average
Rule 12	More	Low	Moderate	Average
Rule 13	Less	Middle	Moderate	Corse
Rule 14	Intermediate	Middle	Moderate	Corse
Rule 15	More	Middle	Moderate	Corse
Rule 16	Less	High	Moderate	Corse
Rule 17	Intermediate	High	Moderate	Corse
Rule 18	More	High	Moderate	Corse
Rule 19	Less	Low	Big	Fine
Rule 20	Intermediate	Low	Big	Fine
Rule 21	More	Low	Big	Fine
Rule 22	Less	Middle	Big	Fine
Rule 23	Intermediate	Middle	Big	Corse
Rule 24	More	Middle	Big	Corse
Rule 25	Less	High	Big	Fine
Rule 26	Intermediate	High	Big	Corse
Rule 27	More	High	Big	Corse

average of the three trials is 154 nm, which is extremely near to the model's expected value for the smallest particle size of 156 nm. Figure 3c displays the particle size of the 8 experiments that are run based on FIS model. Their parameters are given in Table 3.

Figure 4 exhibits a 3D illustration of the two-way interaction of inputs on the particle size. It also shows how fuzzy outperforms the orthogonal system. Because, as FIS modeling considers all possibilities, it allows for knowledge of the conditions that have not been experimentally studied. Figure 4a depicts that at a high filling ratio and lower temperature, a smaller particle size is achieved due to high pressure and low kinetic movement of the particles. Then, Fig. 4b shows that within the interested intervals, independent of the process duration, at lower temperatures, particles with smaller particle size are formed. Additionally, Fig. 4c demonstrates that at a high filling ratio and short process duration, particles with small particle sizes can be fabricated, because prolonged duration at high temperature promotes diffusion resulting in agglomeration, eventually.

3.2 Analysis of variance (ANOVA)

By using MINITAB software v.20, ANOVA analysis is performed to study the individual as well as combined interaction of the parameters onto the particle size and to investigate the most effecting parameter of the hydrothermal reaction. The results are displayed in Table 4.

The calculation reveals that the 3-way interaction of the parameters has less effect on the final product properties, and therefore, this is taken as an error and ANOVA calculations are revised and given in Table 5. The R-square and R-square adjusted values of the revised ANOVA analysis are found to be 99.67% and 97.71%, respectively.

According to the calculations, the most effective parameter is the temperature as it has the biggest F-value. As the temperature rises, the kinetic energy of the molecules increases, leading to more frequent and energetic collisions. Moreover, at higher temperatures, not only does the rate of nucleation increase, resulting in a greater number of particles formation, but also the thermal motion of the molecules is more rapid, leading to faster diffusion, hence to particle growth. At elevated temperatures, the kinetic energy of the particle and their collision with each other get enhanced. As a result, the particlescollide, stick together, and form larger agglomerates. All these factors make the temperature the most effecting parameter in the hydrothermal reaction.

3.3 Material Characterization

3.3.1 Mechanistic understanding of particle formation: crystallization and growth

In a hydrothermal reaction, the formation of nanoparticles involves an ordered nucleation and growth mechanism. In a hydrothermal reaction, the production of nanoparticles begins with nucleation, in which stabilized clusters form, and then grows by autocatalytic surface processes.The regulation of nucleation and growth mechanisms in a hydrothermal synthesis allows for the controlled and precise fabrication of nanoparticles with specific sizes and properties.

During synthesis of nano particle, nucleation takes place in the first place. Nucleation in a hydrothermal reaction requires relatively high supersaturation levels, which mean for the precipitation of metal ions as their oxide, metallic ions must exist in abundance in the solution. The process begins with the formation of clusters, typically on a 0–2 nm scale, which represents crystalline materials. These clusters are referred to embryos and their formation is reversible because of their small size. Therefore, the production of these clusters does not guarantee the initial continuation of the synthesis process. When cluster (embryo) reaches to certain size (critical radius) and critical activation energy, they become irreversible. Upon reaching the critical point,

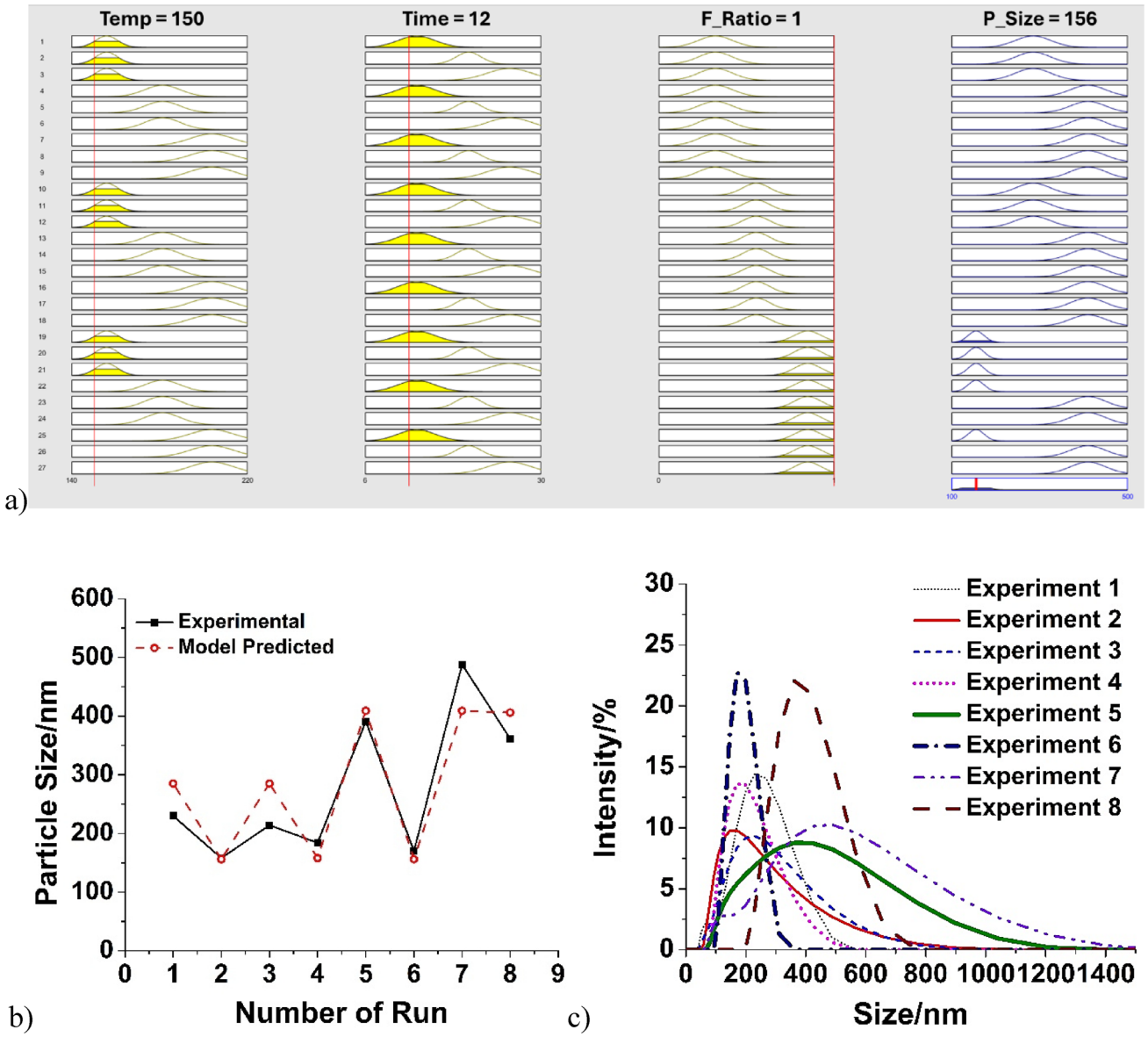

Fig. 3 **a** The rules set by fuzzy based on the given data, **b** Graphical comparison between experimental and model predicted particle size values, **c** Particle size measurements of the 8 experiments

Table 3 The experimental vs the predicted values of 8 runs

	Temperature (°C)	Time (h)	Filling ratio	Experimental particle size (nm)	Calculated particle size (nm)	PRE (%)	SSE
EXP. 1	150	12	0.5	230	285	− 19.2982	0.037242
EXP. 2	150	12	1	158	156	1.265823	0.00016
EXP. 3	150	24	0.5	214	285	− 24.9123	0.062062
EXP. 4	150	24	1	184	158	14.13043	0.019967
EXP. 5	200	12	0.5	391	409	− 4.40098	0.001937
EXP. 6	200	12	1	169.9	156	8.181283	0.006693
EXP. 7	200	24	0.5	488	409	16.18852	0.026207
EXP. 8	200	24	1	361.3	406	− 11.0099	0.012122
Average percentage relative error =						− 2.48	0.16639

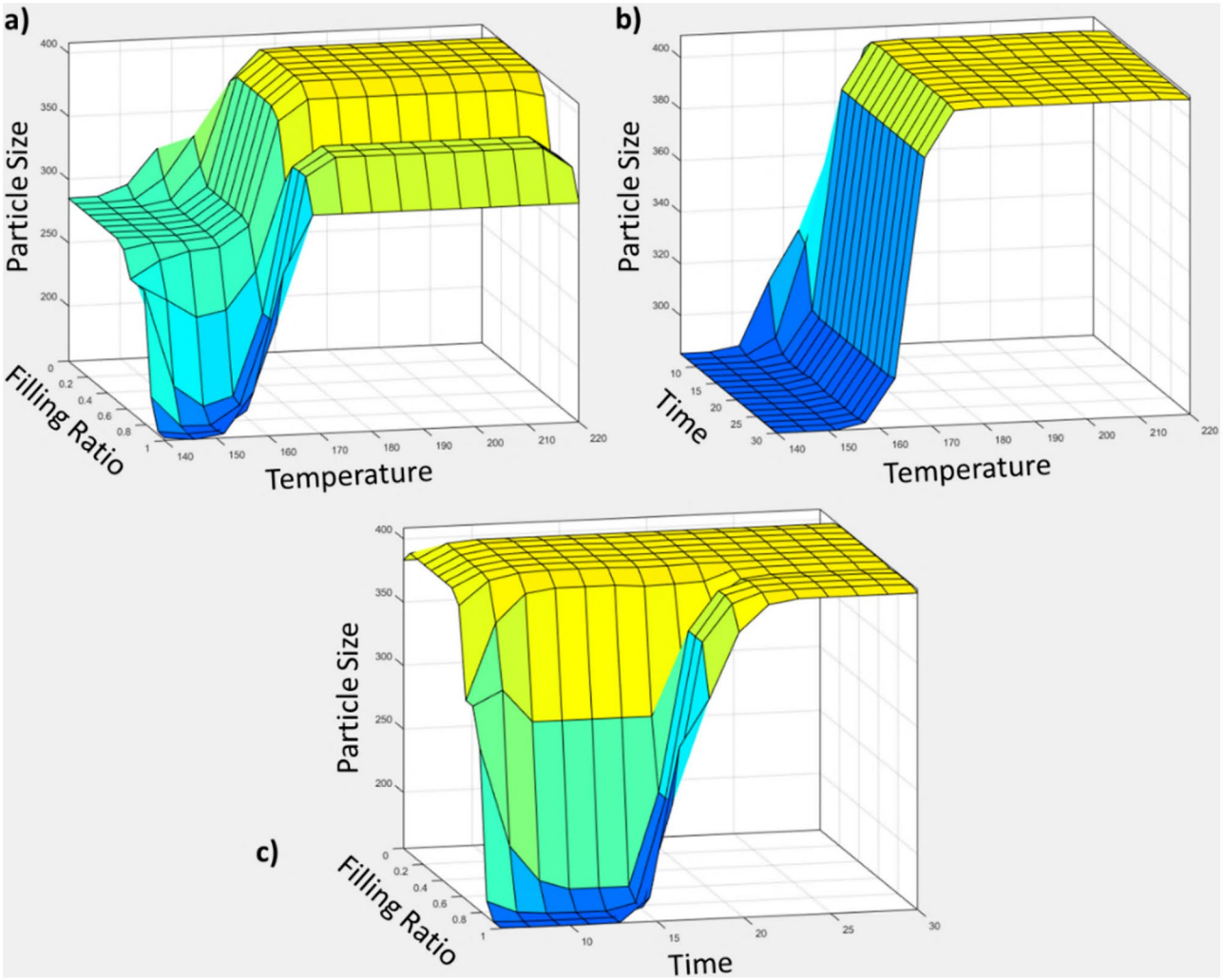

Fig. 4 Surface plots of effect of temperature, time, and filling ratio on particle size

Table 4 ANOVA calculations for particle size of powder

Source	D*f*	Adj SS	Adj MS	*F*-value	*P* value
A (temperature)	1	48,703	48,703.2	–	–
B (time)	1	11,130	11,130.3	–	–
C (filling ratio)	1	25,290	25,290.0	–	–
2-way interactions					
A (temp) × B (time)	1	9688	9688.3	–	–
A (temp) × C (F ratio)	1	7552	7552.2	–	–
B(time) × C (F ratio)	1	2326	2325.6	–	–
3-way interactions					
A (temp) × B (time) × C (F ratio)	1	343	343.2	–	–
Error	0	–	–		
Total	7	105,033			

an irreversible phase change occurs leading to nucleation. Then, these nuclei grow and stabilize, forming the basis for nanoparticle development [55–57].

After the nucleation of nuclei, growth takes place involving fast, autocatalytic surface growth, where the nanoparticles expand through diffusion and stabilization occurs. In the

Table 5 Revised ANOVA calculations for particle size of powder

Source	D*f*	Adj SS	Adj MS	*F*-value	*P* value
A (temperature)	1	48,703	48,703.2	141.90	0.053
B (time)	1	11,130	11,130.3	32.43	0.111
C (filling ratio)	1	25,290	25,290.0	73.68	0.074
2-way interactions					
A (temp) × B (time)	1	9688	9688.3	28.23	0.118
A (temp) × C (F ratio)	1	7552	7552.2	22.00	0.134
B (time) × C (F ratio)	1	2326	2325.6	6.78	0.233
Error	1	343	343.2	–	–
Total	7	105,033			

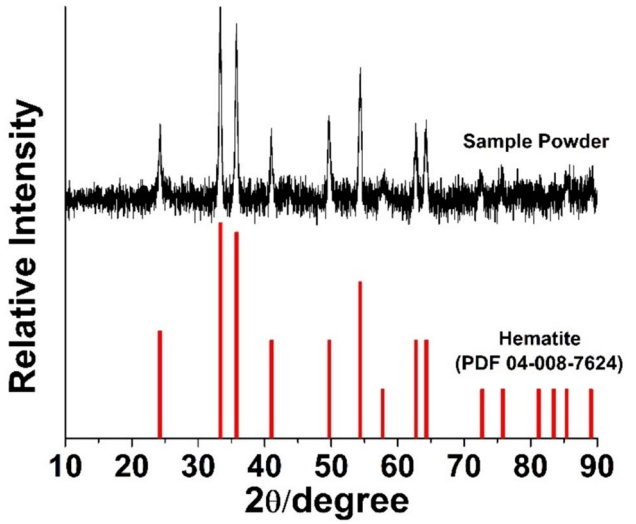

Fig. 5 XRD pattern of the powder fabricated at the defined conditions of fuzzy

case of metallic nanoparticles, the metal cation-containing precursor is reduced or decomposed then atoms combine to form stable nanoparticles, completing the growth process. The hydrothermal approach offers advantages in regulating the rate, uniformity of nucleation, growth, and aging processes, allowing for precise control over the formation of nanoparticles. The size of nanoparticles in a hydrothermal reaction is controlled by the nucleation and grain growth processes, ensuring the desired characteristics and properties of the final nanoparticles [55–57].

However, factors such as reaction temperature, time, and filling ratio have very prominent effects on the synthesized nanoparticles' properties. For instance, the increase in temperature causes aggregation leading to relatively bigger particles. The prolonged reaction duration also results in relative coarsening in grain size. Conversely, the filling ratio has an inverse effect on the particle. Higher filling ratio causes higher pressure averting the particle growth. Therefore, it is important to carefully select the parameters and their levels to obtain particles in nanometric size i.e., time, temperature, and filling ratio.

3.3.2 Powder characterization: the structural and compositional analyses

The XRD pattern of the powder fabricated at the defined conditions by FL reveals that the sample contains hematite (Fig. 5). The chemical compositions of the initial material as well as the fabricated powder are also examined by XRF method. The initial material that belongs to SS grade 304L is very suited to extract the values from it. In this work to coprecipitate Fe, Cr, Ni together in oxide form in one step, the adjustment of pH during precipitation is realized considering Pourbaix diagrams. In the study of Janin et al. [58], they disclosed that at pH above 10, iron and chromium get precipitated together from a leachate as hydroxide, and the fact that Fe and Cr have similar ionic radii (Fe^{+3} 0.67 Å; Cr^{+3} 0.64 Å); after the calcination of this precipitate, a tendency to form a solid solution of iron oxide at any concentration level is increased due to the same crystal structure [59]. Therefore, although no further or additional peak related to chromium oxide is observed in XRD analysis, XRF reveals 16% Cr and 9% Ni existence along with 69%wt. Fe in the powder.

During solid solution, the solute atom (i.e., Cr and Ni) completely takes in the place of the host (i.e., Fe) atom in the oxide structure. Such substitution causes imperfections in the unit cell lead to ion and electron mobility improvements, stabilizing structural phases, and increasing mechanical strength [60–63]. These benefits leading to better charge/discharge cycle, higher specific capacity, and improved durability in energy storage devices. The tailored properties of solid solutions, such as optimized morphology and electrolyte compatibility, contribute to the overall efficiency and longevity of anode material [63, 64].

3.3.3 Electrochemical performances of the anode vs Li

Fabricated anode has been punched and CR2032 standard half-cells are assembled to test the electrochemical performance. 50 mA g^{-1} current load is applied to cycle the cell between 1 mV and 3V vs Li. Figures 6a–c show the electrochemical performance of the electrode. In Figure 6a, a discharge curve located around 0.7 V is assigned to theformation of solid-electrolyte interface (SEI) and the reduction of metal oxide [65, 66]. As reported in the literature, the reduction of metal oxide (i.e., hematite) follows 3 steps given by Eqs. (5–7) [65–67]. Following the first reaction, a small amount of lithium gets inserted in an iron oxide solid solution and forms hexagonal $Li_xFe_2O_3$. Then, upon further lithiation, a change in the crystal structure from hexagonal

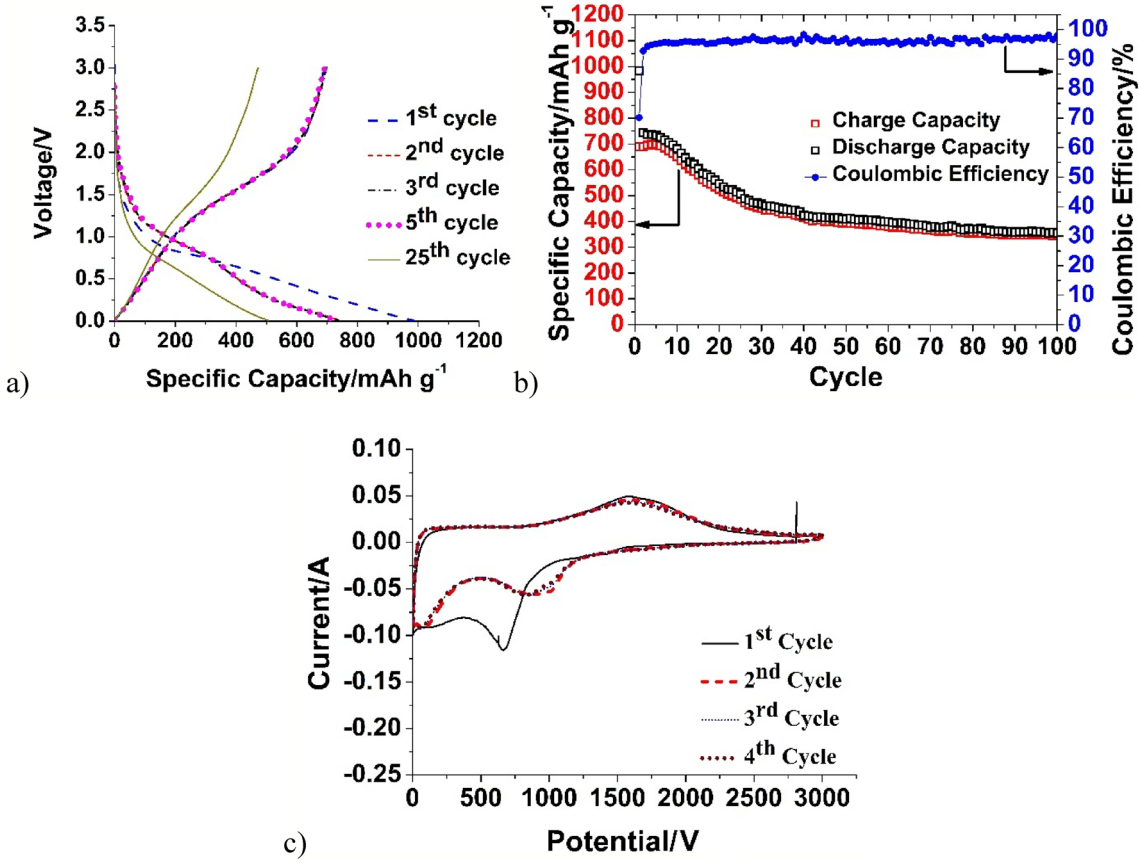

Fig. 6 Electrochemical performance of iron oxide sample **a** Voltage–Capacity curves **b** Capacity–Cycle curves **c** cyclic voltammetry curves

$Li_xFe_2O_3$ to cubic $Li_2Fe_2O_3$ occurs. Finally, a complete reduction of iron oxide happens and a reduced elemental iron cluster in Li_2O matrix is achieved. In charging, the elemental iron is converted to iron oxide following Eq. 8. [65, 66, 68, 69] (Fig. 6a).

$$Fe_2O_3 + xLi^+ + xe^- \leftrightarrow Li_xFe_2O_3 \quad (5)$$

$$Li_xFe_2O_3 + (2-x)Li^+ + (2-x)e^- \leftrightarrow Li_2Fe_2O_3 \quad (6)$$

$$Li_2Fe_2O_3 + 4Li^+ + 4e^- \leftrightarrow 2Fe^0 + 3Li_2O \quad (7)$$

$$Fe_2O_3 + 6Li^+ + 6e^- \leftrightarrow 2Fe + 3Li_2O \quad (8)$$

Figure 6b depicts that a high capacity (983 mAh g^{-1}) is delivered by the electrode, because of the higher theoretical capacity (1006 mAh g^{-1}) of Fe_2O_3 and smallest homogeneous morphology of the fabricated powder. After the 50th cycle, the capacity becomes ~410 mAh g^{-1} with a columbic efficiency of 96%. The decrease in the capacity is due to inevitable volumetric change caused by structural conversion that happened in cycling (see Eqs. 5–8). At this point, this performance shows that the iron oxide-based material synthesized from biomedical waste has successfully completed 100 cycle tests. This superior performance can be explained by the fact that the particle size of the obtained powder is ~150 nm and its structure is designed as a solid solution instead of pure metal oxide.

The cyclic curvatures of the electrode for the first 4 cycles are given in Fig. 6c. The results are in well agreement with previously disclosed outcomes in literature [65, 70, 71]. Herein, a characteristic behavior of hematite is noted, the cathodic peaks at 0.7 V and a wide slight hump appeared at 1.3 V, signifying the irreversible SEI formation and the reduction of hematite with lithium, resulting in the formation of Li_2O and Fe^0 (Eqs. 5–7). In the interim, only a broad peak at about 1.7 V is attributed to the oxidation of iron to Fe^{+3} [65, 68–70].

To understand the prevalent mechanism on the capacity, CV at different scan rates is performed [72]. First, the electrode has been cycled 3 times at 50 mA g^{-1} between 1 mV and 3 V, for the stabilization of the electrode/electrolyte interface. Later, voltammetry is applied with different scan rates of 0.3 mV s^{-1}, 0.5 mV s^{-1}, 1 mV s^1, and 1.5 mV s^{-1} between the same cutoff voltage range 1 mV–3

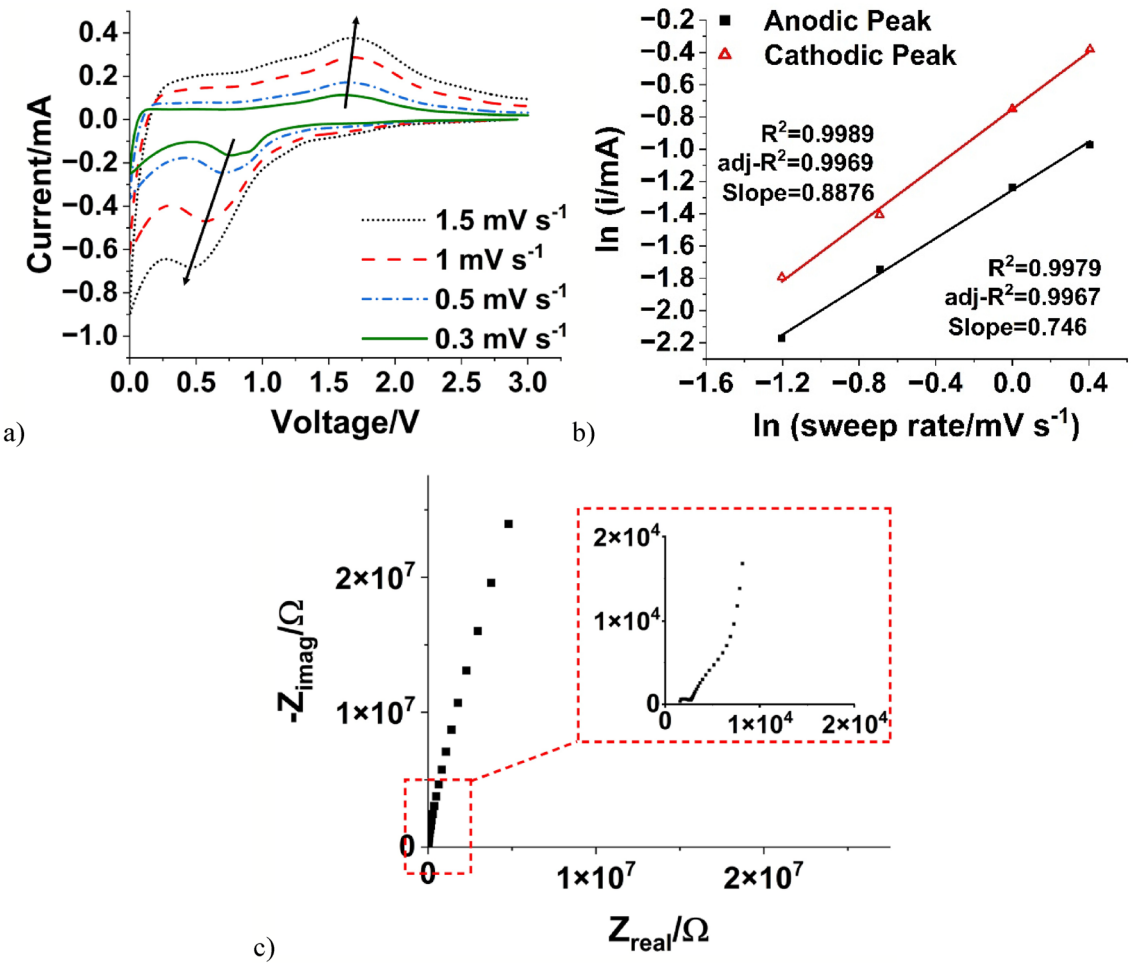

Fig. 7 **a** & **b** Sweep Rate Test **c** electrochemical impedance after 1st discharge of the sample

V (Fig. 7a, b). Then, log of peak current values has been taken and plotted versus scan rate and fitted with the linear model (Fig. 7c, d). In the literature, it is mentioned that the capacitive effect can be quantified using the Eq. 9 [72], where *a* and *b* are constants. The value of *b* is between 0.5 and 1. 0.5 signifying that the reaction is diffusion controlled; while when the value of b is 1, it signifies that the reaction has capacitive control. Figure 7b shows ln (*i*, peak current)-ln (*v*, sweep rate) of two peaks detected at the anodic and cathodic sides of Figure 7a. The fitted line's slope gives b value. Regression analysis of each fitted line shows that the fitting is perfectly done as R^2 and R^2-adj are close to 1. The value of *b* in the current case is between 0.5 and 1, which shows mixed control (Figure 7b). Further Fig. 7c exhibits the impedance results of the electrode after 1st discharge, according to which the electrode shows small charge transfer resistance of the material owing to the small nodular shape morphology of the synthesized iron oxide.

$$k_1 v + k_1 v^{1/2} = a v^b \tag{9}$$

4 Conclusion

In this study, the valorization of biomedical waste has been realized in a high-value-added application such as anode active material in LIB. This point of view will enable the formation of a system in which sectors can achieve mutual gains economically on the way through the generation of a sustainable world.

For the first time in literature, orthodontic waste (stainless steel braces) has been leached through sulfuric acid with 100% efficiency and the leachate has been treated by hydrothermal reaction. Fuzzy logic (FL) has been applied to synthesize particles with optimum size as reported in the literature. Time, temperature, and filling ratio have been selected

as input factors/parameters. The FL model not only provides valuable insights into the effects of process parameters on particle size but also allows for further refinement and consideration of intermediate parameter values. Furthermore, ANOVA analysis yields that the filling ratio and temperature are the two most influencing parameters in the synthesis of iron-oxide-based anode material through the hydrothermal reactional route. The fabricated powder exhibits desirable structural, morphological, and compositional characteristics, and its electrochemical performance as an anode material is promising. The combination of these experimental and modeling approaches can contribute to the development and optimization of materials for energy storage applications.

Acknowledgements The authors greatly acknowledge Istanbul Medipol University Regenerative and Restorative Medicine Research Center for allowing the use of particle size and XRD in characterizations. The authors also thank Alper Yeşilyurt (Arçelik) for the XRF analysis.

Author contributions BD Karahan has contributed to conceptualization, investigation, methodology, supervision, writing—original draft MH Ashraf has contributed to the investigation, visualization, writing—original draft Z Sen has contributed to methodology, writing—review & editing.

Data availability No datasets were generated or analysed during the current study.

Declarations

Conflict of interest BD Karahan used to work at Istanbul Medipol University which sponsored the realization and characterization of the experiments. Istanbul Technical University is the current affiliation of the corresponding author.

References

1. Herrington G (2021) Update to limits to growth: comparing the World3 model with empirical data. J Ind Ecol 25(3):614–626. https://doi.org/10.1111/JIEC.13084
2. Ding Y, Cano ZP, Yu A, Lu J, Chen Z (2019) Automotive Li-ion batteries: current status and future perspectives. Electrochem Energy Rev 2(1):1–28. https://doi.org/10.1007/S41918-018-0022-Z
3. Qadrdan M, Jenkins N, Wu J (2018) Smart grid and energy storage. In: McEvoy's handbook of photovoltaics: fundamentals and applications, p. 915–928, https://doi.org/10.1016/B978-0-12-809921-6.00025-2
4. Energy Storage Market Report (2020) Department of energy. https://www.energy.gov/energy-storage-grand-challenge/downloads/energy-storage-market-report-2020. Accessed 14 Nov 2022
5. Usai L, Lamb JJ, Hertwich E, Burheim OS, Strømman AH (2022) Analysis of the Li-ion battery industry in light of the global transition to electric passenger light duty vehicles until 2050. Environ Res: Infrastruct Sustain 2(1):011002. https://doi.org/10.1088/2634-4505/AC49A0
6. Francis CFJ, Kyratzis IL, Best AS (2020) Lithium-ion battery separators for ionic-liquid electrolytes: a review. Adv Mater. https://doi.org/10.1002/ADMA.201904205
7. Korthauer R (2018) Lithium-ion batteries: basics and applications. Springer, Luxembourg, pp 1–413
8. Davidsson Kurland S (2019) Energy use for GWh-scale lithium-ion battery production. Environ Res Commun 2(1):012001. https://doi.org/10.1088/2515-7620/AB5E1E
9. Ellingsen LAW, Majeau-Bettez G, Singh B, Srivastava AK, Valøen LO, Strømman AH (2014) Life cycle assessment of a lithium-ion battery vehicle pack. J Ind Ecol 18(1):113–124. https://doi.org/10.1111/JIEC.12072
10. Dunn JB, Gaines L, Sullivan J, Wang MQ (2012) Impact of recycling on cradle-to-gate energy consumption and greenhouse gas emissions of automotive lithium-ion batteries. Environ Sci Technol 46(22):12704–12710. https://doi.org/10.1021/ES302420Z/SUPPL_FILE/ES302420Z_SI_001.PDF
11. Majeau-Bettez G, Hawkins TR, StrØmman AH (2011) Life cycle environmental assessment of lithium-ion and nickel metal hydride batteries for plug-in hybrid and battery electric vehicles. Environ Sci Technol 45(10):4548–4554. https://doi.org/10.1021/ES103607C/SUPPL_FILE/ES103607C_SI_001.PDF
12. Kim HC, Wallington TJ, Arsenault R, Bae C, Ahn S, Lee J (2016) Cradle-to-gate emissions from a commercial electric vehicle li-ion battery: a comparative analysis. Environ Sci Technol 50(14):7715–7722. https://doi.org/10.1021/ACS.EST.6B00830/SUPPL_FILE/ES6B00830_SI_001.PDF
13. Berckmans G, Messagie M, Smekens J, Omar N, Vanhaverbeke L, Van Mierlo J (2017) Cost projection of state of the art lithium-ion batteries for electric vehicles up to 2030. Energies 10(9):1314. https://doi.org/10.3390/EN10091314
14. Lain MJ (2001) Recycling of lithium ion cells and batteries. J Power Sources 97–98:736–738. https://doi.org/10.1016/S0378-7753(01)00600-0
15. Gülcan MF, Karahan BD (2022) Upcycling of industrial iron scale waste for reutilization as anode material in lithium ion batteries. Mater Chem Phys. https://doi.org/10.1016/J.MATCHEMPHYS.2021.125270
16. Zhao Q, Li W, Liu C, Jiang M, Saxén H, Zevenhoven R (2023) Preparation of anode material of lithium-ion battery by spent pickling liquor. J Sustain Metall 9(1):148–159. https://doi.org/10.1007/S40831-022-00638-1/FIGURES/15
17. Ashraf H, Karahan BD (2023) Electroless nickel-plated ferrochromium flue dust as anode material for lithium-ion batteries. J Mater Eng Perform. https://doi.org/10.1007/S11665-022-07772-7
18. Zhang D et al (2022) Rational design of fly ash-based composites for sustainable lithium-ion battery anodes. Electrochim Acta 410:140035. https://doi.org/10.1016/J.ELECTACTA.2022.140035
19. Liu H et al (2019) High-performance α-Fe_2O_3/C composite anodes for lithium-ion batteries synthesized by hydrothermal carbonization glucose method used pickled iron oxide red as raw material. Compos B Eng 164:576–582. https://doi.org/10.1016/J.COMPOSITESB.2019.01.084
20. Hua Luo S, Bei Hu D, Liu H, Zhe Li J, Yi TF (2019) Hydrothermal synthesis and characterization of α-Fe_2O_3/C using acid-pickled iron oxide red for Li-ion batteries. J Hazard Mater 368:714–721. https://doi.org/10.1016/J.JHAZMAT.2019.01.106
21. Li Y, Mao J, Xie H, Li J (2018) Heat-treatment recycling of waste toner and its applications in lithium ion batteries. J Mater Cycles Waste Manag 20(1):361–368. https://doi.org/10.1007/S10163-017-0599-Z/METRICS
22. Wang L, Wei Z, Mao M, Wang H, Li Y, Ma J (2019) Metal oxide/graphene composite anode materials for sodium-ion batteries. Energy Storage Mater 16:434–454. https://doi.org/10.1016/J.ENSM.2018.06.027
23. Bin Wu H, Chen JS, Hng HH, Lou XW (2012) Nanostructured metal oxide-based materials as advanced anodes for lithium-ion batteries. Nanoscale 4(8):2526–2542. https://doi.org/10.1039/C2NR11966H

24. Zhang J, Yu A (2015) Nanostructured transition metal oxides as advanced anodes for lithium-ion batteries. Sci Bull (Beijing) 60(9):823–838. https://doi.org/10.1007/S11434-015-0771-6
25. Courtel FM, Duncan H, Abu-Lebdeh Y, Davidson IJ (2011) High capacity anode materials for Li-ion batteries based on spinel metal oxides AMn_2O_4 (A = Co, Ni, and Zn). J Mater Chem 21(27):10206–10218. https://doi.org/10.1039/C0JM04465B
26. Müller J, Michalowski P, Kwade A (2023) Impact of silicon content and particle size in lithium-ion battery anodes on particulate properties and electrochemical performance. Batteries 9(7):377. https://doi.org/10.3390/BATTERIES9070377/S1
27. Je M, Han DY, Ryu J, Park S (2023) Constructing pure Si anodes for advanced lithium batteries. Acc Chem Res 56(16):2213–2224. https://doi.org/10.1021/ACS.ACCOUNTS.3C00308/ASSET/IMAGES/LARGE/AR3C00308_0006.JPEG
28. Liu T et al (2024) Recycled micro-sized silicon anode for high-voltage lithium-ion batteries. Nat Sustain 7(8):1057–1066. https://doi.org/10.1038/s41893-024-01393-9
29. Liang C, Gao M, Pan H, Liu Y, Yan M (2013) Lithium alloys and metal oxides as high-capacity anode materials for lithium-ion batteries. J Alloys Compd 575:246–256. https://doi.org/10.1016/J.JALLCOM.2013.04.001
30. Qi W, Shapter JG, Wu Q, Yin T, Gao G, Cui D (2017) Nanostructured anode materials for lithium-ion batteries: principle, recent progress and future perspectives. J Mater Chem A Mater 5(37):19521–19540. https://doi.org/10.1039/C7TA05283A
31. Abe Y, Saito I, Tomioka M, Kabir M, Kumagai S (2022) Effects of excessive prelithiation on full-cell performance of Li-ion batteries with a hard-carbon/nanosized-Si composite anode. Batteries 8(11):210. https://doi.org/10.3390/BATTERIES8110210
32. Zhao H et al (2024) Si-based anodes: advances and challenges in li-ion batteries for enhanced stability. Electrochem Energy Rev 7(1):1–36. https://doi.org/10.1007/S41918-024-00214-Z
33. Luo F et al (2015) Thick solid electrolyte interphases grown on silicon nanocone anodes during slow cycling and their negative effects on the performance of Li-ion batteries. Nanoscale 7(17):7651–7658. https://doi.org/10.1039/C5NR00045A
34. Lu M, Cheng H, Yang Y (2008) A comparison of solid electrolyte interphase (SEI) on the artificial graphite anode of the aged and cycled commercial lithium ion cells. Electrochim Acta 53(9):3539–3546. https://doi.org/10.1016/J.ELECTACTA.2007.09.062
35. Zhao Z et al (2015) Formation of curcumin nanoparticles via solution-enhanced dispersion by supercritical CO_2. Int J Nanomedicine 10:3171. https://doi.org/10.2147/IJN.S80434
36. Rangappa R, Rajoo S (2019) Effect of thermo-physical properties of cooling mass on hybrid cooling for lithium-ion battery pack using design of experiments. Int J Energy Environ Eng 10(1):67–83. https://doi.org/10.1007/S40095-018-0284-6/TABLES/11
37. Zadeh LA (1973) Outline of a new approach to the analysis of complex systems and decision processes. IEEE Trans Syst Man Cybern. https://doi.org/10.1109/TSMC.1973.5408575
38. Zadeh LA (1977) Fuzzy sets and their application to pattern classification and clustering analysis. In: Classification and clustering, p. 251–299, https://doi.org/10.1016/B978-0-12-714250-0.50014-0
39. Ross TJ (2010) Fuzzy logic with engineering applications: third edition. https://doi.org/10.1002/9781119994374
40. Mamdani EH (1977) Application of fuzzy logic to approximate reasoning using linguistic synthesis. IEEE Trans Comput. https://doi.org/10.1109/TC.1977.1674779
41. Takagi T, Sugeno M (1985) Fuzzy identification of systems and its applications to modeling and control. IEEE Trans Syst Man Cybern. https://doi.org/10.1109/TSMC.1985.6313399
42. Huang Z, Hahn J (2009) Fuzzy modeling of signal transduction networks. Chem Eng Sci. https://doi.org/10.1016/j.ces.2009.01.041
43. Dutta Majumder D, Karan S, Goswami A (2011) Synthesis and characterization of gold nanoparticles—a fuzzy mathematical approach. Lect Notes Comput Sci (Incl Subser Lect Notes Artif Intell Lect Notes Bioinform). https://doi.org/10.1007/978-3-642-21786-9_53/COVER
44. Shetty R, Hegde A (2022) Taguchi based fuzzy logic model for optimisation and prediction of surface roughness during AWJM of DRCUFP composites. Manuf Rev (Les Ulis) 9:2. https://doi.org/10.1051/MFREVIEW/2021027
45. Hosseini Asl SM, Masomi M, Hosseini M, Javadian H, Ruiz M, Sastre AM (2017) Synthesis of hydrous iron oxide/aluminum hydroxide composite loaded on coal fly ash as an effective mesoporous and low-cost sorbent for Cr(VI) sorption: fuzzy logic modeling. Process Saf Environ Prot 107:153–167. https://doi.org/10.1016/J.PSEP.2017.02.012
46. Tonnes of COVID-19 health care waste expose urgent need to improve waste management systems. https://www.who.int/news/item/01-02-2022-tonnes-of-covid-19-health-care-waste-expose-urgent-need-to-improve-waste-management-systems. Accessed: 19 Nov 2022
47. Tan X et al (2023) Investigation of addition of calcium phosphate ceramic to multilayer scaffold for bone applications with improved mechanical properties: fuzzy logic analysis. Ceram Int 49(5):8339–8349. https://doi.org/10.1016/J.CERAMINT.2022.10.366
48. Allison T (2007) Doctor blades. Gravure 21(1):32–35. https://doi.org/10.1007/978-0-387-88953-5_10/COVER
49. Burns JC et al (2011) Introducing symmetric Li-ion cells as a tool to study cell degradation mechanisms. J Electrochem Soc 158(12):A1417. https://doi.org/10.1149/2.084112JES/XML
50. Yoo PS, Lee BW, Liu C (2015) Effects of pH value, reaction time, and filling pressure on the hydrothermal synthesis of $ZnFe_2O_4$ nanoparticles. IEEE Trans Magn. https://doi.org/10.1109/TMAG.2015.2434380
51. Tehrani FS, Ahmadian H, Aliannezhadi M (2020) Hydrothermal synthesis and characterization of WO_3 nanostructures: effect of reaction time. Mater Res Express 7(1):015911. https://doi.org/10.1088/2053-1591/AB66FC
52. Ataie A, Piramoon MR, Harris IR, Ponton CB (1995) Effect of hydrothermal synthesis environment on the particle morphology, chemistry and magnetic properties of barium hexaferrite. J Mater Sci 30(22):5600–5606. https://doi.org/10.1007/BF00356692/METRICS
53. Hakuta Y, Ura H, Hayashi H, Arai K (2005) Effects of hydrothermal synthetic conditions on the particle size of γ-AlO(OH) in sub and supercritical water using a flow reaction system. Mater Chem Phys 93(2–3):466–472. https://doi.org/10.1016/J.MATCHEMPHYS.2005.03.047
54. Şen Z (2017) Innovative trend methodologies in science and engineering. https://doi.org/10.1007/978-3-319-52338-5/COVER
55. Prathan A et al (2020) Controlled structure and growth mechanism behind hydrothermal growth of TiO_2 nanorods. Sci Rep 10(1):1–11. https://doi.org/10.1038/s41598-020-64510-6
56. Bakken K, Grendal OG, Einarsrud MA (2023) In situ characterisation for studying nucleation and growth of nanostructured materials and thin films during liquid-based synthesis. J Solgel Sci Technol 105(2):596–605. https://doi.org/10.1007/S10971-022-05974-Y
57. Khalil M, Yu J, Liu N, Lee RL (2014) Hydrothermal synthesis, characterization, and growth mechanism of hematite nanoparticles. J Nanopart Res 16(4):1–10. https://doi.org/10.1007/S11051-014-2362-X
58. Zhang G et al (2015) Solid-solution-like ZnO/C composites as excellent anode materials for lithium ion batteries. Electrochim Acta. https://doi.org/10.1016/j.electacta.2015.10.133

59. Benny S, Grau-Crespo R, De Leeuw NH (2009) A theoretical investigation of α-Fe_2O_3–Cr_2O_3 solid solutions. Phys Chem Chem Phys 11(5):808–815. https://doi.org/10.1039/B815907F
60. Helmers L et al (2021) Sustainable solvent-free production and resulting performance of polymer electrolyte-based all-solid-state battery electrodes. Energ Technol 9(3):2000923. https://doi.org/10.1002/ENTE.202000923
61. Zhao S et al (2024) Research progress on the solid electrolyte of solid-state sodium-ion batteries. Electrochem Energy Rev. https://doi.org/10.1007/s41918-023-00196-4
62. Mishra K et al (2018) Submicro-sized Si–Ge solid solutions with high capacity and long cyclability for lithium-ion batteries. J Mater Res 33(11):1553–1564. https://doi.org/10.1557/JMR.2018.145
63. Li S, Ling M, Qiu J, Han J, Zhang S (2015) Anchoring ultra-fine TiO_2–SnO_2 solid solution particles onto graphene by one-pot ball-milling for long-life lithium-ion batteries. J Mater Chem A Mater 3(18):9700–9706. https://doi.org/10.1039/C5TA01350J
64. Mengesha TH, Beshahwured SL, Hendri YB, Walle KZ, Wu YS, Yang CC (2024) Improved electrochemical performance of solid-state lithium metal batteries with stable SEI and CEI layers via in situ formation technique. J Mater Chem A Mater. https://doi.org/10.1039/d3ta07835c
65. Lu F et al (2013) Comparative investigation of the performances of hematite nanoplates and nanograins in lithium-ion batteries. Phys Chem Chem Phys. https://doi.org/10.1039/c3cp50619c
66. Wang Z, Luan D, Madhavi S, Hu Y, Lou XW (2012) Assembling carbon-coated α-Fe_2O_3 hollow nanohorns on the CNT backbone for superior lithium storage capability. Energy Environ Sci 5(1):5252–5256. https://doi.org/10.1039/C1EE02831F
67. Bin Wu H, Chen JS, Hng HH, Lou XW (2012) Nanostructured metal oxide-based materials as advanced anodes for lithium-ion batteries. Nanoscale. https://doi.org/10.1039/c2nr11966h
68. Tian B et al (2013) Combined surface and electrochemical study of the lithiation/delithiation mechanism of the iron oxide thin-film anode for lithium-ion batteries. J Phys Chem C 117(42):21651–21661. https://doi.org/10.1021/JP4064438/ASSET/IMAGES/MEDIUM/JP-2013-064438_0007.GIF
69. Yao X, Tang C, Yuan G, Cui P, Xu X, Liu Z (2011) Porous hematite (α-Fe_2O_3) nanorods as an anode material with enhanced rate capability in lithium-ion batteries. Electrochem commun 13(12):1439–1442. https://doi.org/10.1016/J.ELECOM.2011.09.015
70. Monnier A et al (2005) α-Fe_2O_3 nanotubes in gas sensor and lithium-ion battery applications. Adv Mater 17(5):582–586. https://doi.org/10.1002/ADMA.200401101
71. Zhao Y, Li J, Ding Y, Guan L (2011) Single-walled carbon nanohorns coated with Fe_2O_3 as a superior anode material for lithium ion batteries. Chem Commun. https://doi.org/10.1039/c1cc12171e
72. Duan H, Du L, Zhang S, Chen Z, Wu S (2019) Superior lithium-storage properties derived from a high pseudocapacitance behavior for a peony-like holey Co_3O_4 anode. J Mater Chem A Mater. https://doi.org/10.1039/c9ta00294d